In Situ Observation of Dark Current Emission in a High Gradient rf Photocathode Gun

Jiahang Shao, Jiaru Shi, Sergey P. Antipov, Sergey V. Baryshev, Huaibi Chen, Manoel Conde, Wei Gai, Gwanghui Ha, Chunguang Jing, Faya Wang, and Eric Wisniewski

Phys. Rev. Lett. **117**, 084801 — Published 15 August 2016

DOI: 10.1103/PhysRevLett.117.084801

In situ observation of dark current emission in a high gradient rf photocathode gun

Jiahang Shao,[1,2,*] Jiaru Shi,[1] Sergey P. Antipov,[2,3] Sergey V. Baryshev,[2,3] Huaibi Chen,[1] Manoel Conde,[2] Wei Gai,[2] Gwanghui Ha,[2] Chunguang Jing,[2,3,†] Faya Wang,[4] and Eric Wisniewski[2]

[1] *Department of Engineering Physics, Tsinghua University Beijing 100084, P.R.China*
[2] *Argonne National Laboratory, Lemont, IL 60439, USA*
[3] *Euclid Techlabs LLC, Bolingbrook, IL 60440, USA*
[4] *SLAC National Accelerator Laboratory, Menlo Park, CA 94025, USA*

(Dated: June 21, 2016)

Undesirable electron field emission (a.k.a. dark current) in high gradient rf photocathode guns deteriorates the quality of photoemission current and limits the operational gradient. To improve the understanding of dark current emission, a high-resolution (∼100 μm) dark current imaging experiment has been performed in an L-band photocathode gun operating at ∼100 MV/m of surface gradient. Scattered strong emission areas with high current have been observed on the cathode. The field enhancement factor, β, of selected regions on the cathode has been measured. The post scanning electron microscopy (SEM) and white light interferometer (WLI) surface examinations reveal the origins of ∼75% strong emission areas overlap with the spots where rf breakdown have occurred.

Electrons can tunnel through a surface barrier modified by the presence of an electric field, resulting in a field emission (FE) current [1–4]. While the existence of this physical phenomenon allows the operation of field emission electron sources [5–8], it has a negative (parasitic) impact on the performance of vacuum resonator-based dc and rf systems such as traveling wave tubes, photocathode guns, and particle accelerators [3, 9–12]. The troublesome field emission current is referred to as dark current. It is an unwanted source of electrons that impacts the energy budget of a device, and is a source of undesired secondary electrons and ions [9, 13, 14]. Historically, dark current has been considered to be a trigger of breakdown in vacuum devices which may interrupt the normal operation of the device and even jeopardize the entire facility [3, 4].

To date many questions surrounding FE still remain, especially in the rf case which limit the improvement of cold cathode electron sources and high gradient accelerators for TeV-scale linear colliders [15] and compact X-ray electron sources [16, 17]. For example, a large discrepancy exists between properties of emission area obtained through direct observation using advanced surface analysis tools and those indirectly obtained from fitting the experimental data to the Fowler-Nordheim (F-N) equation [3, 18]; the temporal evolution of the FE area under high electromagnetic fields is mostly unknown [19]; and empirical methods and procedures to suppress or enhance dark current lack theoretical support. All these questions result from the lack of a means for *in situ* high-resolution FE observation. In earlier FE studies under a dc field, emission mapping with better than 1 μm resolution has been achieved by scanning an anode along the cathode [20–22]. However, imaging the emission areas at high resolution while they are emitting under an rf field is extremely challenging due to the wide emitting phase (the timing with respect to the applied rf field) and energy spread range of the dark current [13, 23–25]. In this Letter, we present observations of *in situ* dark current emission in a high gradient photocathode gun using a dedicated dark current imaging beamline.

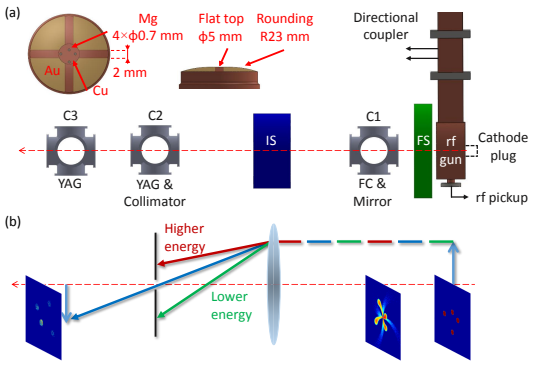

FIG. 1. The dark current imaging system at AWA. (a) The designed cathode with a reference pattern and the beamline layout: FC, Faraday Cup; C, vacuum Cross to house imaging components which were mounted on retractable actuators; FS, Focusing Solenoid; IS, Imaging Solenoid; and YAG, doped Yttrium Aluminum Garnet phosphor screen. Inset: Top and side view of the novel shaped cathode with its sputtering pattern. (b) The equivalent optical imaging system. Insets: ASTRA simulation results for the emission patterns on the cathode, at the gun exit, and in the imaging plane.

The study was conducted at Argonne Wakefield Accelerator facility (AWA). The imaging beamline is shown in Fig. 1(a) [26]. To achieve high-resolution dark current imaging, a method to select electrons from certain emitting phases and narrow the energy spread was developed using external axial magnetic fields (i.e. solenoids) and a collimator at the focal plane. The object being imaged was a novel-shaped copper cathode in a 1.3 GHz rf gun. The cathode is ∼20 mm in diameter with a large edge rounding and a small flat center (inset, Fig. 1(a)) to enhance FE on the top area. ∼100 nm thick magnesium and gold (Mg has a work function of 3.7 eV, Au 5.1 eV,

and Cu 4.6 eV) have been sputtered in certain areas to create a spatial pattern as a reference. The diameter of four magnesium spots is 0.7 mm and their positions in polar coordinates are (0.8 mm, 0), (2.2 mm, $\pi/2$), (2.2 mm, π), and (1.5 mm, $3\pi/2$), respectively. Electrons emitted from the cathode gain energy from the rf gun depending on the emitting phase. They are accordingly focused by the solenoids at different longitudinal positions. The transverse positions of electrons depend on their emission phases, applied focusing forces, and their initial transverse emitting angles on the cathode (the longitudinal direction is along the beamline axis) [27]. Thus, a blurred pattern is formed at the exit of the gun and deteriorates downstream, as simulated by the beam dynamics code ASTRA [28]. When a collimator with a small aperture is applied after the focusing elements, only electrons with the proper focusing position and energy gain are allowed to pass through. A sharp image can be then obtained. The whole imaging system also can be considered as an optical system, as illustrated in Fig. 1(b).

The average magnification and rotation of the imaging system can be defined as

$$\begin{cases} \overline{mag} = \dfrac{\overline{\rho}}{\rho_0} \\ \overline{rot} = \overline{\varphi} - \varphi_0 \end{cases}$$

where (ρ_0,φ_0) is the initial emitting position on the cathode in polar coordinates, (ρ,φ) is the image position on the last YAG screen (C3 in Fig. 1(a)) of electrons emitted at different phases and initial transverse angles, and $\overline{\rho}$ and $\overline{\varphi}$ are the average value of ρ and φ. As the system is axial symmetry, the resolution can be defined in radial and angular direction. Assuming ρ and φ follow the Gaussian distribution, the resolutions are defined as

$$\begin{cases} R_\rho = 2.35 \times \dfrac{\delta_\rho}{\overline{mag}} \\ R_\varphi = 2.35 \times \delta_\varphi \rho_0 \end{cases}$$

where δ_ρ and δ_φ are the standard deviation of ρ and φ. The resolutions improve when smaller apertures are imposed.

Four 60 μm thick apertures at a 30 mm spatial interval are mounted on a stainless steel plate which can be precisely moved along the transverse direction by a motorized actuator so as to choose different apertures. The diameters of the apertures are 8 mm, 1 mm, 0.5 mm, and 0.2 mm, respectively. Based on the simulations, 40$\sim$140 μm resolutions can be achieved depending on the initial FE electron emittance when the smallest aperture is applied [27].

Diagnostics used in the experiment are a bidirectional coupler to monitor the input and reflected rf signals, an antenna (rf pickup probe) to monitor the rf signal inside the cavity, and a mirror to roughly locate breakdown positions during rf conditioning. The YAG screens are placed perpendicular to the beam line and the image is transported out of the beamline in the transverse direction by a mirror angled at 45° and located behind each screen. A PI-MAX Intensified CCD (ICCD) camera [29] is used to capture the image with 47 μm/pixel resolution on the last YAG screen. Given $\overline{mag} = 5$, the camera resolution at the cathode is 9.4 μm/pixel which does not limit the imaging quality of the whole system.

Before the imaging experiment, the electric field on the cathode (noted as E_c) has been carefully conditioned to 120 MV/m with $\sim$2.5 MW input power (pulse length was 6.5 μs and repetition rate was 5 Hz). The total pulses for conditioning was $\sim$135000 and the breakdown rate was controlled to be $\sim 10^{-3}$/pulse. Judged by the flash observed on the mirror [30], breakdowns occurred on the cathode and inside the cavity. After the conditioning, E_c was lowered to 105 MV/m. Steady dark current emission regions on the metal surface were observed and no further breakdowns occurred on those areas during the experiment which lasted for $\sim$50000 pulses.

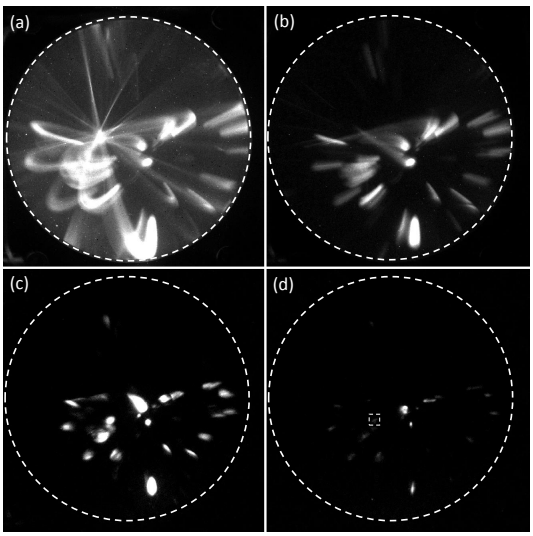

FIG. 2. Dark current images on the last YAG screen. The white dashed circle indicates the boundary of the YAG screen. The white dashed square in (d) indicates the emission area for the resolution calculation. (a) Without collimator. (b-d) With collimator. The aperture diameters are 8 mm, 1 mm, and 0.2 mm, respectively. (a-b) Accumulation of 20 frames. (c-d) Accumulation of 100 frames.

Typical dark current images on the last YAG screen are shown in Fig. 2. Other than FE electrons through the aperture, the brightness on the YAG screen also can be affected by the background luminance originating from X-rays generated by the energetic electrons, secondary electrons, light reflection along the beamline, etc. To quantify the background, dark current images were taken with a blank stainless steel plate. Then the background was subtracted from the image taken with the aperture present to ensure that brightness is only caused by the

FE current through the aperture.

The imaging quality improves with smaller apertures, which validates the high-resolution dark current imaging method in rf structures by emitting phase and energy selection. Each bright spot in Fig. 2(d) corresponds to a strong emission area on the cathode. Within an emission area, tiny micro-structures (defined as emitters) that can not be distinguished by the system may exist and they contribute to the luminance. For simplicity, we assume these emitters are identical and located uniformly within an emission area whose size is ($d\rho$, $d\varphi$). Electrons from each emitter follow the Gaussian distribution of δ_ρ and δ_φ on the last YAG screen. Then the root-mean-square (rms) size of the bright sport on the imaging YAG screen can be calculated as

$$\begin{cases} \rho_{rms} = \sqrt{\delta_\rho^2 + \overline{mag}^2 d\rho^2/12} > \delta_\rho \\ \varphi_{rms} = \sqrt{\delta_\varphi^2 + d\varphi^2/12} > \delta_\varphi \end{cases}$$

Thus, taking the size of a small bright spot as marked in Fig. 2(d), the upper limits of the axial and angular system resolution are calculated to be 147 μm and 107 μm, respectively.

Strong emissions from unpredicted spots rather than the pre-defined pattern have been discovered. Most of these emission areas were traced back to rf breakdown areas shown by the *ex situ* surface examination. Despite a nominal lower work function with respect to copper and gold, strong FE from the magnesium spots was not observed. Oxidization of the magnesium layer during the cathode installation which could raise its work function may be accountable [31].

To date the F-N equation is the most commonly used convention to quantitatively describe FE [1–4]. Four determinants of the emission current are taken into account: the applied electric field strength, the emission area size A_e, the material work function ϕ, and the field enhancement factor β. In previous studies of rf structures, β is usually measured as an average value for a large surface [3, 8, 18, 26]. With the imaging system, β can further measured for localized regions by quantifying their variation in luminous intensity with the rf field.

The brightness of the dark current image is proportional to the energy deposited on the YAG screen (luminance of the YAG screen has a linear response to the deposited energy). Along with other known parameters, the field enhancement factor β of selected areas can be obtained by fitting to the F-N equation [3]. During the measurement, E_c was varied from 105 MV/m to 70 MV/m and the solenoid current was adjusted accordingly to maintain the same emitting positions on the last YAG screen. In order to minimize the dependence of the capture ratio (defined as the current that can pass through the aperture divided by the total emission current from the cathode) on E_c, the biggest aperture (8 mm in diameter) was applied in this measurement. Though the resolutions are reduced (∼1 mm), separated strong emission areas (bright spots) can still be distinguished. The background caused by other sources was measured and subtracted at each field level.

β for the entire imaged area is 76 which falls into the typical range in previous studies [10, 18]. Small regions which covers strong emission areas are chosen for localized β measurement. As a comparison, regions of the same size are also selected on the dark part inside and outside the YAG screen (illustrated in Fig. 3(a)) for weak emission area and background, respectively. Results are shown in Fig. 3(b). The low value and nonlinear dependence of data for the background confirms the brightness due to other sources has been subtracted correctly. β of the strong and weak emission areas is discovered to be similar. In fact, β of other bright spots and dark areas as shown in Fig. 3(a) varies from 70 to 90 which is insignificant compared with the variation in brightness.

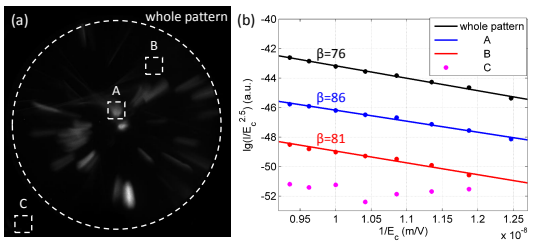

FIG. 3. Field enhancement factor measurement by the dark current imaging system. The white dashed circle indicates the boundary of the YAG screen. (a) Dark current image with the biggest aperture. White dashed squares (610 μm × 610 μm on the cathode) indicate selected regions for the measurement as shown in (b). A: strong emission area, B: weak emission area, and C: background. A and B both locate on the copper surface by the *ex situ* examination. (b) Fowler-Nordheim plot. Spots and lines are the measured data and linear fitting, respectively.

In order to have a quantitative explanation, a simple model of the strong and weak emission areas is adopted as shown in Fig. 4(a). In a weak emission area we assume it contains numbers of N weak emitters which have the similar emission size $A_{e,0}$ and field enhancement factor β_0. In a strong emission area, besides numbers of weak emitters, it contains at least one strong emitter with $A_{e,1} = \alpha N A_{e,0}$ and β_1. I_0, I_1, I_{weak}, and I_{strong} denote to the emission current from the weak emitter, the strong emitter, the weak emission area, and the strong emission area, respectively. β of the weak emission area is equal to β_0. Meanwhile, β of the strong emission area (noted as β_{strong}) fitted by the F-N equation is weighted by β_0, β_1, and α. For the measured β_0 of 81 and I_{strong}/I_{weak} of ∼300, the dependence of α on β_1 is plotted as the blue line in Fig. 4(b). With each calculated (α, β_1) pair, β_{strong} is plotted as the red line in Fig. 4(b). As $I_{strong} \gg I_{weak}$, $I_1 \gg NI_0$ and β_{strong} is nearly equal

to β_1. With β_{strong} is measured to be 86, β_1 and α can be obtained from the plots in Fig. 4(b) to be ∼86 and ∼160, respectively. The high α also indicates the remarkable difference in brightness between the weak and strong emission areas is caused by A_e when β is similar and ϕ is the same.

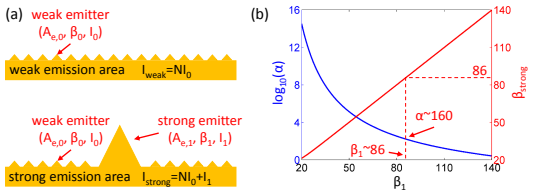

FIG. 4. Comparison between strong and weak emission areas. (a) Model of the strong and weak emission areas. (b) α of the strong emitter (blue) and β_{strong} (red) versus β_1.

After the imaging experiment, the cathode was examined by SEM and WLI as illustrated in Fig. 5(a-e). The major part of the surface remains intact and the roughness is 10-20 nm. Meanwhile, ∼40 breakdown spots have been observed within the areas as marked by the red circles in Fig. 5(a). Micro-structures such as melting craters and droplets are clearly signatures of the breakdown spots [3], which likely lead to large A_e. To study the relationship between the strong emission areas and the breakdown spots, the dark current image obtained with the smallest aperture has been resized and rotated based on the $\overline{mag}$ and $\overline{rot}$ simulated by the ASTRA code. The results show that ∼75% of the strong emission areas overlap with the breakdown spots, as illustrated in Fig. 5(f). The origin of the remaining ∼25% strong emission areas remains unknown. They may be attributed to microscopic surface features such as grain boundaries or defects that are not detected by the examination tools used. The results also reveal that half of the breakdown spots do not emit current at a level high enough to be detected by the imaging system.

In previous study, a significant increase of dark current has been observed after rf breakdowns and it implies that FE may result from rf breakdowns in high gradient rf cavities [3]. The overlap of strong dark current emission areas and breakdown spots supports this conventional understanding. Besides, FE is generally considered to be a trigger of rf breakdown [3, 4]. However, the observation that no further breakdowns occurred at the strong dark current emission areas in the imaging system indicates that a steady FE alone may not be sufficient to trigger an rf breakdown.

In summary, a high-resolution dark current imaging setup has been developed based on an L-band photocathode gun. Separated strong emission areas have been observed with ∼100 μm resolution. The localized field enhancement factor has been measured. The results have been analyzed with a new model of emission area. Post

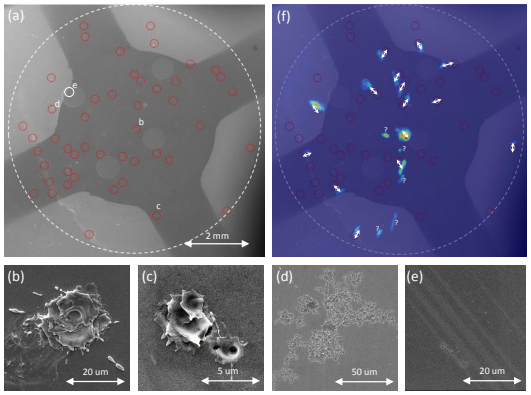

FIG. 5. Overlap of strong dark current emission areas and breakdown spots. (a) Overview of breakdown spots on the cathode. The red circles indicate the areas which contain breakdown spots. The white dash circle indicates the maximum visible range by the dark current imaging system. (b-e) Zoom-in view of circles marked in (a). (b, c) Breakdown spot on Cu which overlaps and does not overlap with a strong dark current emission area, respectively. (d) Breakdown spot on Au which overlaps with a strong dark current emission area. (e) Smooth undamaged surface on Mg. (f) Overlap of the strong dark current emission areas and the breakdown spots. The dark current imaging is in false color for better display. The overlapped strong emission areas and breakdown spots are marked by arrows. The strong emission areas with unknown origin are marked by the question mark.

surface analysis by SEM and WLI reveals that ∼75% of the strong dark current emission areas overlap with the rf breakdown spots. This work greatly expands the understanding of field emission which in turn benefits research into electron sources, particle accelerators, and high gradient rf devices in general.

We would like to thank the Tsinghua University machine shop for preparing the new shaped cathodes, all staff in the AWA group for their work in the experiment, Dr. Klaus Flöttmann from DESY for his great help with the ASTRA code and other useful discussions, and Paul Schoessow of Euclid TechLabs for his valuable comments on the manuscript. The work by the AWA group is funded through the U.S. Department of Energy Office of Science under Contract No. DE-AC02-06CH11357. The work at Tsinghua University is supported by National Natural Science Foundation of China under Grant No. 11135004. The work by F. Wang is supported by the U.S. Department of Energy Early Career Research Program under Contract Code LAB 11-572. SEM measurements were conducted in the Electron Microscopy Center of the Center for Nanoscale Materials at Argonne National Laboratory. Use of the Center for Nanoscale Materials, an Office of Science user facility, was supported by the U. S. Department of Energy, Office of Science, Office of Basic Energy Sciences, under Contract No. DE-AC02-06CH11357.

* shaojh07@mails.tsinghua.edu.cn
† jingchg@anl.gov

[1] R. H. Fowler and L. Nordheim, Proc. R. Soc. London, Ser. A **119**, 173 (1928).
[2] J. Gadzuk and E. Plummer, Rev. Mod. Phys. **45**, 487 (1973).
[3] J. W. Wang and G. A. Loew, SLAC Report No. **7684** (1997).
[4] G. N. Fursey, *Field Emission in Vacuum Microelectronics* (Springer US, 2005).
[5] K. B. Teo, E. Minoux, L. Hudanski, F. Peauger, J.-P. Schnell, L. Gangloff, P. Legagneux, D. Dieumegard, G. A. Amaratunga, and W. I. Milne, Nature **437**, 968 (2005).
[6] X. Li, M. Li, L. Dan, Y. Liu, and C. Tang, Phys. Rev. ST Accel. Beams. **16**, 123401 (2013).
[7] P. Piot, C. Brau, B. Choi, B. Blomberg, W. Gabella, B. Ivanov, J. Jarvis, M. Mendenhall, D. Mihalcea, H. Panuganti, *et al.*, Appl. Phys. Lett. **104**, 263504 (2014).
[8] S. V. Baryshev, S. Antipov, J. Shao, C. Jing, K. J. P. Quintero, J. Qiu, W. Liu, W. Gai, A. D. Kanareykin, and A. V. Sumant, Appl. Phys. Lett. **105**, 203505 (2014).
[9] J. H. Han, M. Krasilnikov, and K. Flöttmann, Phys. Rev. ST Accel. Beams **8**, 033501 (2005).
[10] A. Grudiev, S. Calatroni, and W. Wuensch, Phys. Rev. ST Accel. Beams. **12**, 102001 (2009).
[11] A. Descoeudres, Y. Levinsen, S. Calatroni, M. Taborelli, and W. Wuensch, Phys. Rev. ST Accel. Beams. **12**, 092001 (2009).
[12] F. Wang, C. Adolphsen, and C. Nantista, Phys. Rev. ST Accel. Beams. **14**, 010401 (2011).
[13] R. Xiang, A. Arnold, T. Kamps, P. Lu, P. Michel, P. Murcek, H. Vennekate, G. Staats, and J. Teichert, Phys. Rev. ST Accel. Beams. **17**, 043401 (2014).
[14] R. Huang, D. Filippetto, C. F. Papadopoulos, H. Qian, F. Sannibale, and M. Zolotorev, Phys. Rev. ST Accel. Beams **18**, 013401 (2015).
[15] *CLIC Conceptual Design Report*, Tech. Rep. (CERN).
[16] H. Tanaka, M. Yabashi, T. Asaka, Y. Asano, N. Azumi, T. Bizen, H. Ego, K. Fukami, T. Fukui, Y. Furukawa, *et al.*, Nature Photon. **6**, 540 (2012).
[17] *SwissFEL Conceptual Design Report*, Tech. Rep. (PSI).
[18] H. Chen, Y. Du, W. Gai, A. Grudiev, J. Hua, W. Huang, J. G. Power, E. E. Wisniewski, W. Wuensch, C. Tang, L. Yan, and Y. You, Phys. Rev. Lett. **109**, 204802 (2012).
[19] J. Shao, H. Chen, W. Gai, C. Jing, J. Shi, F. Wang, and L. Xiao, in *Proceeding of IPAC2014, Dresden, Germany*, THPRI077 (2014).
[20] R. J. Noer, P. Niedermann, N. Sankarraman, and O. Fischer, J. Appl. Phys. **59**, 3851 (1986).
[21] D. Lysenkov and G. Müller, Int. J. Nanotechnol **2**, 239 (2005).
[22] A. Dangwal Pandey, G. Müller, D. Reschke, and X. Singer, Phys. Rev. ST Accel. Beams. **12**, 023501 (2009).
[23] J. Han, J. Bähr, H. Grabosch, M. Krasilnikov, V. Miltchev, A. Oppelt, and B. Petrosyan, in *Proceedings of PAC2005, Knoxville, USA* (2005) pp. 895–897.
[24] A. Moretti, Z. Qian, J. Norem, Y. Torun, D. Li, and M. Zisman, Phys. Rev. ST Accel. Beams **8**, 072001 (2005).
[25] D. Dowell, E. Jongewaard, C. Limborg-Deprey, J. Schmerge, and A. Vlieks, in *Proceedings of PAC2007, Albuquerque, New Mexico, USA* (2007) pp. 1299–1301.
[26] J. Shao, S. P. Antipov, S. V. Baryshev, H. Chen, M. Conde, D. S. Doran, W. Gai, C. Jing, W. Liu, J. Power, *et al.*, Phys. Rev. Lett. **115**, 264802 (2015).
[27] J. Shao, H. Chen, J. Shi, X. Wu, W. Gai, C. Jing, S. Antipov, and F. Wang, in *Proceeding of IPAC2016, Busan, Korea*, TUPOW014 (2016).
[28] K. Flöttmann, *ASTRA-A space charge tracking algorithm*, DESY.
[29] *PI-MAX/PI-MAX2 System*, Princeton Instruments (2004).
[30] W. Wuensch, in *Proceeding of EPAC2002, Paris, France* (2002) pp. 134–138.
[31] J. Y. Lim, J. S. Oh, B. D. Ko, J. W. Cho, S. O. Kang, G. Cho, S. U. Han, and E. H. Choi, J. of Appl. Phys. **94**, 764 (2003).